

Pulsars versus Dark Matter Interpretation of ATIC/PAMELA

Dmitry Malyshev,^{*} Ilias Cholis,[†] and Joseph Gelfand[‡]

Center for Cosmology and Particle Physics

4 Washington Place, Meyer Hall of Physics,

NYU, New York, NY 10003

(Dated: May 10, 2022)

We study the flux of electrons and positrons injected by pulsars and by annihilating or decaying dark matter. We argue that at high energies, above several hundred GeV, the flux from a collection of pulsars should have large fluctuations around an average curve whereas the flux from dark matter should be smooth. The presence or absence of significant fluctuations can be used as a model independent way to distinguish between the two possibilities. A pedagogical review of electron and positron emission from pulsars is given.

Contents		B. Review of pulsars	14
I. Introduction	2	C. Smoothing due to spatial variation in energy losses	17
II. Single pulsar flux	3	D. Constraining properties of pulsars and ISM	18
A. Properties of the interstellar medium	3	References	22
B. Green function for diffusion-loss propagation	4		
C. Flux from a single pulsar	4		
III. Flux from a distribution of pulsars	6		
A. Continuous distribution of pulsars	6		
B. Statistical cutoff	7		
C. Fluctuations around continuous distribution flux	8		
IV. Flux from Dark Matter	10		
V. Conclusions and outlook	11		
A. A roadmap for possible outcomes of cosmic rays experiments	12		
A. Electron and positron backgrounds	13		

^{*}Electronic address: dm137@nyu.edu; On leave of absence from ITEP, Moscow, Russia, B. Cheremushkinskaya 25

[†]Electronic address: ijc219@nyu.edu

[‡]Electronic address: jg168@astro.physics.nyu.edu; National Science Foundation Astronomy and Astrophysics Postdoctoral Fellow

I. INTRODUCTION

Several cosmic ray experiments show an excess of electrons and positrons over the expected background at high energies. The PAMELA experiment reports a higher positron ratio in the energies 10 – 100 GeV [1]. The ATIC experiment shows a bump in the total flux of electrons and positrons over the background at energies above 100 GeV and below 1 TeV [2] (see also PPB-BETS [3]). The HESS collaboration measured electrons and positrons between 700 GeV and 4 TeV [4] and its results are compatible with those of ATIC.

The anomalies in ATIC and PAMELA data have inspired a lot of discussion on possible sources of high energy electrons and positrons. This source must be closer than a few kiloparsecs (kpc) otherwise the injected electrons would lose their energy due to the synchrotron radiation and inverse Compton scattering (ICS) during propagation. Two viable possibilities are dark matter [5][6][7][8][9][10][11][12] and pulsars [13][14][15][16].

Both explanations give reasonable fits to ATIC and PAMELA data and the problem of distinguishing between these possibilities is difficult to solve [17][18]. This problem has two parts: large statistical errors in the data and significant theoretical uncertainties in the DM and pulsar models. In this paper, we address the problem of the theoretical uncertainties and propose a model independent way to distinguish pulsars from the DM using the local e^+e^- fluxes (Zhang et al [19] suggested a possible way to distinguish the two possibilities using the gamma-rays and radio frequency photons from the central part of the Galaxy).

We argue that, due to “cooling” of electrons during propagation, only a few young pulsars can contribute at energies $E \sim 1$ TeV. As a result, at these energies the flux of electrons should have specific bumps or steps corresponding to individual pulsars. There is a maximal cutoff energy defined by the age of the youngest pulsar within about 3 kpc. Below this cutoff there is a first bump due to the electrons from the youngest pulsar, after that there is a second bump due to the electrons from the second youngest pulsar and so on. We will show that at lower energies the bumps become

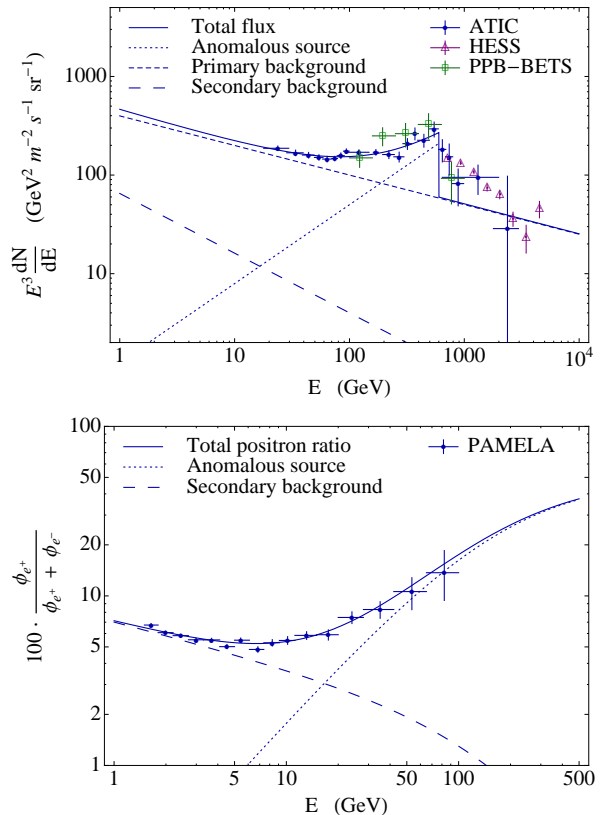


FIG. 1: Power-law fit to ATIC and PAMELA data. The best fit for the additional source of electrons and positrons is $F \sim E^{-n_a}$ with $n_a = 2.2$ and $\chi^2/dof = 42/26$. In this fit we introduce a sharp cutoff at 600 GeV and use the ATIC points below 600 GeV and all PAMELA points. HESS and PPB-BETS data are shown for comparison.

so close that it is impossible to resolve them and the flux looks like a smooth curve.

In general, the ATIC and PAMELA data can be fitted if we assume an additional power law flux of electrons and positrons below some cutoff energy. The e^+e^- backgrounds at high energies scale as roughly E^{-3} [20]. We write the total electron+positron flux from the additional source in the form

$$E^3 \frac{dN_a}{dE} = f_a \left(\frac{E}{E_0} \right)^{3-n_a} \quad (1)$$

where we choose the reference energy $E_0 = 100$ GeV. The normalization coefficient $f_a \equiv E_0^3 F(E_0)$ and the

index n_a are the two fit parameters. In the fits we use ATIC and PAMELA data simultaneously. The best fits with $\chi^2/dof < 3$ are obtained for

$$\begin{aligned} n_a &= 2.2 \pm 0.2 \\ f_a &= (50 \pm 10) \text{ GeV}^2 \text{ m}^{-2} \text{ s}^{-1} \text{ sr}^{-1} \end{aligned} \quad (2)$$

These values show little dependence on the cutoff region $E \gtrsim 600$ GeV. In the fits we use a sharp cutoff at 600 GeV and ignore the ATIC points above 600 GeV. Similar results are obtained if we take all ATIC points and introduce a break in the power law or an exponential cutoff.

In Figure 1 we use a simple power law fluxes for the backgrounds. The primary background is proportional to $E^{-3.3}$ and the secondary background is proportional to $E^{-3.6}$. This is a good approximation in the energy range $10 \text{ GeV} < E < 1\text{TeV}$ [20][21]. Outside these energies the indexes of the backgrounds change. In Appendix A we consider a more realistic background and find that the values in (2) are insensitive to the background choice.

Thus the properties of the additional flux necessary to fit the data have little dependence on either the background choice or the cutoff region. Any physical model that can provide a power law flux of electrons with parameters given in Equation (2) and a cutoff above 600 GeV will automatically fit the data. In this paper, we analyze the flux from annihilating Dark Matter, from a single pulsar, and from a continuous distribution of pulsars. We find that one can choose the parameters in these models such that the corresponding fluxes have the form of a power-law with parameters (2) and a break above 600 GeV. As we summarize in the concluding section, these fluxes can look very similar to each other and could be impossible to distinguish.

We will argue that a model independent way to distinguish pulsars from DM is to look for the features at high energies. We expect to see a few bumps in the flux from the pulsars whereas the DM flux is generally expected to be smooth with a single cutoff.

II. SINGLE PULSAR FLUX

The flux of electrons at the Earth depends on both the spectrum of injected electrons and the properties of the interstellar medium (ISM). At first, we review the propagation in the ISM and then derive the fluxes from pulsars and dark matter.

A. Properties of the interstellar medium

The ISM contains a random magnetic field with the field strength on the order of $3\mu\text{G}$. The corresponding Larmor radius for a 1 TeV electron, $r = \frac{pc}{eB} < 10^{-3}$ pc, is much smaller than the correlation length of the magnetic field. Consequently, the electrons mostly follow magnetic field lines on a random path. For ultrarelativistic particles, the diffusion coefficient is [21]

$$D(E) = D_0 \left(\frac{E}{E_0} \right)^\delta, \quad (3)$$

where $\delta = 0.3 - 0.6$ and $D_0 = (3 - 5) \times 10^{28} \text{ cm}^2 \text{ s}^{-1}$ for $E_0 = 1$ GeV. We find it convenient to write the diffusion coefficient in terms of the energy rather than the magnetic rigidity, $R \equiv \frac{p}{q}$, where p is the momentum and q is the charge of the particle. In our case, the two definitions are equivalent.

As electrons propagate in the ISM, they lose energy. For $E \gtrsim 5$ GeV the dominant loss mechanisms are synchrotron radiation and inverse Compton scattering off Cosmic Microwave Background (CMB), infrared (IR), and starlight photons. The corresponding energy losses are

$$\dot{E} \equiv -b(E) = -b_0 E^2 \quad (4)$$

where $b_0 = 1.6 \times 10^{-16} \text{ GeV}^{-1} \text{ s}^{-1}$ for the local density of photons and $B = 3 \mu\text{G}$.

Before we present a formal solution to the propagation problem let us define a few characteristic numbers. In estimations, it is convenient to represent the parameters in the units of $\text{pc} = 3 \times 10^{18} \text{ cm}$ and $\text{kyr} = 3 \times 10^{10} \text{ s}$. In this paper we will usually use $b_0 = 1.6 \times 10^{-16} \text{ GeV}^{-1} \text{ s}^{-1} = 5 \times 10^{-6} \text{ GeV}^{-1} \text{ kyr}^{-1}$ and $D_0 = 3 \times 10^{28} \text{ cm}^2 \text{ s}^{-1} = 100 \text{ pc}^2 \text{ kyr}^{-1}$ with $\delta = 0.4$. We

can integrate Equation (4) in order to find the energy difference in terms of the electron travel time

$$\frac{1}{E_1} - \frac{1}{E_0} = b_0 t \quad (5)$$

where E_0 is the initial energy of the electron and E_1 is the energy at time t . The *cooling break* is defined as the maximal energy that an electron can have if it has traveled during time t

$$E_{cb} = \frac{1}{b_0 t} \quad (6)$$

The characteristic travel time is therefore

$$t \gtrsim 100 \text{ kyr} \quad \text{for} \quad E \lesssim 2 \text{ TeV}. \quad (7)$$

The characteristic distance an electron travels before cooling to energy E is the diffusion distance $x_{diff}^2 = 4D(E)t$, where $t = \frac{1}{b_0 E}$,

$$x_{diff} \lesssim 5 \text{ kpc} \quad \text{for} \quad E \gtrsim 10 \text{ GeV}. \quad (8)$$

B. Green function for diffusion-loss propagation

In general, the evolution of the energy density of electrons moving in random paths and losing energy can be described by the following diffusion-loss equation [22][23]

$$\frac{\partial \rho}{\partial t} = \frac{\partial}{\partial E} (b(E)\rho) + D(E) \frac{\partial^2 \rho}{\partial \mathbf{x}^2} + Q(\mathbf{x}, E, t). \quad (9)$$

where $Q = \frac{dN}{dE dt d^3x}$ is the energy density of the source. In principle, one can also take into account reacceleration, convection, and decays (collisions), but for electrons with $E > 10$ GeV these contributions can be ignored.

The general solution to Equation (9) is found in [22][24]. In order to solve Equation (9) for a general source, one can introduce the Green function $G(\mathbf{x}, E, t; \mathbf{x}_0, E_0, t_0)$ satisfying

$$\frac{\partial G}{\partial t} - \frac{\partial}{\partial E} (b(E)G) - D(E) \frac{\partial^2 G}{\partial x^2} = \delta(\mathbf{x} - \mathbf{x}_0) \delta(E - E_0) \delta(t - t_0). \quad (10)$$

Then, the solution to (9) is

$$\rho(\mathbf{x}, E, t) = \int d^3 \mathbf{x}_0 \int dE_0 \int dt_0 G(\mathbf{x}, E, t; \mathbf{x}_0, E_0, t_0) \cdot Q(\mathbf{x}_0, E_0, t_0). \quad (11)$$

The Green function can be found as follows. One can define the variables $t' = t - \tau$ and λ [22][24], where

$$\tau \equiv \tau(E, E_0) = \int_E^{E_0} \frac{dE'}{b(E')} \quad (12)$$

$$\lambda \equiv \lambda(E, E_0) = \int_E^{E_0} \frac{D(E') dE'}{b(E')} \quad (13)$$

The variable $t'(t, E)$ is invariant with respect to the differential operator $\partial_t - b(E)\partial_E$. In fact, $D^{-1}(E)(\partial_t - b(E)\partial_E) = \partial_\lambda$ and Equation (10) becomes the usual diffusion equation in λ and \mathbf{x} . The Green function is then [22][24]

$$G(\mathbf{x}, E, t; \mathbf{x}_0, E_0, t_0) = \frac{1}{b(E)} \frac{1}{(4\pi\lambda)^{3/2}} e^{-\frac{(\mathbf{x}-\mathbf{x}_0)^2}{4\lambda}} \cdot \delta(t - t_0 - \tau) \theta(E_0 - E) \quad (14)$$

Equation (9) and the above Green function have a few limitations. The magnetic field and the densities of IR and starlight photons depend on the point in space, consequently the diffusion coefficient and the energy loss function depend on the coordinates: $D = D(E, \mathbf{x})$, $b = b(E, \mathbf{x})$, and there is no simple analytic solution in this case. In Appendix C we calculate corrections to e^+e^- spectrum at the Earth due to spatial variations in energy losses.

C. Flux from a single pulsar

With the general Green function in hand, one can find the density of electrons at any point in space for any source. In this section we derive the flux from a single pulsar.

The distances to pulsars are sufficiently large that we can assume they are point sources. We assume that most of the pulsars' rotational energy is lost via magnetic dipole radiation [25] which eventually transforms into the energy of electrons and positrons:

$$Q_{pulsar}(\mathbf{x}, E, t) = Q(E) \frac{1}{\tau} \left(1 + \frac{t}{\tau}\right)^{-2} \delta(\mathbf{x}) \quad (15)$$

Note that the pulsar time scale τ in this formula and the variable introduced in (12) are unrelated. We review the derivation of this formula in Appendix B.

At late times, the spin-down luminosity scales as t^{-2} and most of the energy is emitted during $t \sim \tau$. The pulsar time scale, $\tau \lesssim 10$ kyr, is much smaller than the typical time scale for electron propagation, $t \gtrsim 100$ kyr. Consequently we can take the limit $\tau \rightarrow 0$

$$\frac{1}{\tau} \left(1 + \frac{t}{\tau}\right)^{-2} \Big|_{\tau \rightarrow 0} \longrightarrow \delta(t) \quad (16)$$

We will assume that the energy spectrum of particles injected into the ISM, $Q(E)$, has the form

$$Q(E) = Q_0 E^{-n} e^{-\frac{E}{M}} \quad (17)$$

where n is the index of the spectrum, M is the cutoff, and Q_0 is the overall normalization. We denote the initial rotational energy of the pulsar by W_0 and define η to be the conversion efficiency of this energy into e^+e^- . Then the total energy emitted in e^+e^- is

$$\int Q(E) E dE = \eta W_0. \quad (18)$$

For $n < 2$, this gives

$$Q_0 = \frac{\eta W_0}{\Gamma(2-n) M^{2-n}}. \quad (19)$$

As we review in Appendix **B**, the electrons emitted from a pulsar are trapped for some time in its Pulsar Wind Nebula (PWN). The index n and the cutoff M of the electron spectrum can be derived from observations of the synchrotron radiation and the ICS photons coming from the PWN. These parameters may vary significantly depending on the pulsars. We argue in Appendix **B** that $n = 1.6 \pm 0.2$ and $M \sim 10$ TeV are reasonable values.

The overall normalization is more difficult to derive, because the initial rotational energy is not known for most of the pulsars. There are models that give an order of magnitude estimate, but their results are highly uncertain [26]. If the age of the pulsar is known independently, then the initial rotational energy can be estimated more robustly. In Appendix **B** we consider the Crab pulsar which is associated with the 1054 supernova explosion and estimate $W_0 \approx 3 \times 10^{50}$ erg. The Crab pulsar is believed to be more energetic than an average pulsar. We will take $W_0 \sim 10^{50}$ erg as the mean initial rotational energy.

Let us now discuss the conversion coefficient η . The energy density near the surface of the pulsar is dominated by the magnetic field and the spin-down luminosity is dominated by the magnetic dipole radiation. In the PWN the energy density is particle dominated, i.e. by the time the radiation reaches the PWN it is mostly converted to the energy of the particles and $\eta \sim 1$ at this stage (see, e.g., [27] for a discussion of the Crab PWN). The problem is that the particles do not immediately escape to the interstellar medium (ISM) but become trapped inside the PWN by its magnetic field. In Appendix **B** we estimate that $\eta \sim 0.1$ due to cooling of the particles before they reach the ISM. This value is model dependent, and can vary greatly from one pulsar to another.

The density of electrons from a pulsar at the Earth can be found by substituting the source function $Q(\mathbf{x}, E, t)$ into Equation (11)

$$\rho(\mathbf{x}, E, t) = \frac{b(E_0)}{b(E)} \frac{1}{(4\pi\lambda)^{3/2}} e^{-\frac{\mathbf{x}^2}{4\lambda}} Q(E_0), \quad (20)$$

where parameter λ is defined in Equation (13) and E_0 is the initial energy of the electrons that cool down to E in time t

$$E_0 = \frac{E}{1 - Eb_0 t}. \quad (21)$$

The density in Equation (20) has a cutoff at the cooling break, $E = \frac{1}{b_0 t}$, since $Q(E_0) \rightarrow 0$ for $E_0 \rightarrow \infty$.

For a density ρ of relativistic particles, the flux is defined as

$$F = \frac{c}{4\pi} \rho. \quad (22)$$

The time evolution of the flux from a single pulsar is shown in Figure 2. Initially, it has a smooth shape with an exponential suppression since the electrons haven't had time to diffuse to Earth. After that, the flux grows and the cutoff moves to the left due to cooling. With time, the flux decreases, as the electrons diffuse over a bigger volume, the cutoff moves further to the left and becomes sharper.

For energies much smaller than the cooling break we can neglect the energy losses. In this case, $E_0 \approx E$, $\lambda \approx D(E)t$ and Equation (20) reduces to

$$\rho(\mathbf{x}, E, t) = \frac{1}{(4\pi D(E)t)^{3/2}} e^{-\frac{\mathbf{x}^2}{4D(E)t}} Q(E). \quad (23)$$

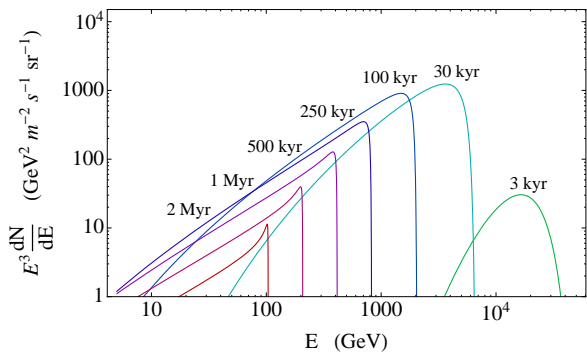


FIG. 2: Time evolution of e^+e^- flux on Earth from a Geminga-like pulsar at a distance of 0.5 kpc. We assume the delta-function approximation for the emission from the pulsar, $Q(\mathbf{x}, E, t) = Q(E)\delta(\mathbf{x})\delta(t)$. The flux from a young pulsar (the 3 kyr curve on the right) has an exponential suppression because the electrons haven't had enough time to diffuse from the pulsar to the Earth. The inner (red) curve is the flux from a $t = 2$ Myr pulsar. The cutoff moves to the left due to cooling of electrons and becomes sharper. After reaching a maximal value, the flux decreases since the electrons diffuse over a large volume.

Assuming that $\mathbf{x}^2 \ll 4D(E)t$, the flux for $E \ll \frac{1}{b_0 t}$ is

$$F(E) = \frac{c}{4\pi} \frac{Q_0}{(4\pi D_0 t)^{3/2}} E^{-n-\frac{3}{2}\delta}. \quad (24)$$

The corresponding fit parameters f_a and n_a are

$$f_a = \frac{c}{4\pi} \frac{Q_0}{(4\pi D_0 t)^{3/2}} E_0^{3-n-\frac{3}{2}\delta},$$

$$n_a = n + \frac{3}{2}\delta.$$

The cutoff energy is defined by the cooling break $E_{cut} = \frac{1}{b_0 t}$.

For a pulsar with an age $t = 200$ kyr the best fit value of f_a can be obtained for $\eta W_0 \approx 3 \times 10^{49}$ erg. If the initial rotational energy is $W_0 = 10^{50}$ erg, then the conversion efficiency is $\eta \approx 0.3$. The index $n_a = 2.2$ can be obtained, for example, for $n = 1.6$ and $\delta = 0.4$. We use these values of parameters for the time evolution of the flux in Figure 2. We also use these parameters in the concluding section, where we compare the flux from a single pulsar with the flux from a distribution of pulsars and the flux from annihilating DM.

Although the possibility that the ATIC and PAMELA anomalies are due to a single pulsar is not excluded, it is unlikely that the flux from a single pulsar is larger than the flux from all the other pulsars. In the next section, we will study the case that the flux of electrons and positrons comes from a collection of pulsars.

III. FLUX FROM A DISTRIBUTION OF PULSARS

In this section we derive the e^+e^- flux from a continuous distribution of pulsars and compare it with the flux from randomly generated collections of pulsars. The continuous distribution flux provides a good approximation at low energies, where a lot of pulsars contribute. At high energies, the ‘‘small number’’ effects become more significant and the flux from pulsars can have significant deviations from the average flux.

A. Continuous distribution of pulsars

We assume that pulsars are homogeneously spread over the Galactic plane and are born at a constant rate N_b [26]. Consequently, the averaged source function is constant in time, localized in the vertical direction, and homogeneous in the Galactic plane

$$Q_{distr}(\mathbf{x}, E, t) = J_0 E^{-n} e^{-\frac{E}{M}} \delta(z) \quad (25)$$

with the normalization constant

$$J_0 = \frac{\eta W_0}{\Gamma(2-n)M^{2-n}} \frac{N_b}{A_{Gal}} \quad (26)$$

where A_{Gal} is the Galaxy area.

The diffusion distance in (8) is significantly smaller than the distance from the Earth to the edge of the Galactic plane [26], $x_{diff} < 10$ kpc, and we can neglect the effects of having an edge at a finite distance.

Using the general Green function in Equation (14), the flux of electrons from this distribution is

$$F = \frac{c}{4\pi} \int d^3\mathbf{x}_0 \int dE_0 \int dt_0 G(\mathbf{x}, E, t; \mathbf{x}_0, E_0, t_0) \cdot Q(\mathbf{x}_0, E_0, t_0). \quad (27)$$

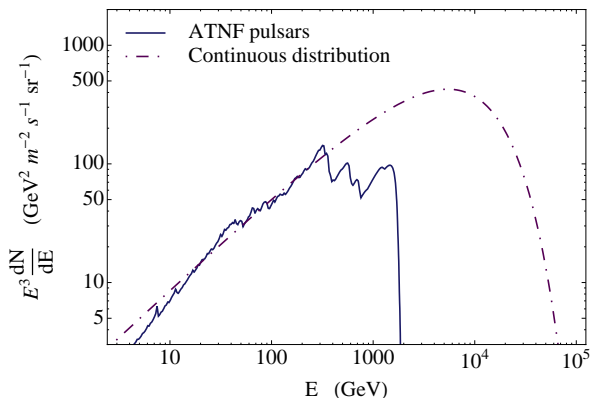


FIG. 3: Continuous distribution versus the ATNF catalog pulsars [28] (see text for the discussion of assumptions and parameters). Several hundred pulsars contribute below 300 GeV and the continuous distribution provides a good approximation for these energies. Above 300 GeV, there is only of order 10 contributing pulsars. The fluctuations in the flux become significant above 300 GeV. The reason for the discrepancy above 2 TeV is discussed in Section III B.

Integrating over t_0 and \mathbf{x} , we obtain

$$F(E) = \frac{c}{4\pi b(E)} \int_E^\infty dE_0 \frac{1}{\sqrt{4\pi\lambda(E, E_0)}} J_0 E_0^{-n} e^{-\frac{E_0}{M}} \quad (28)$$

where λ is defined in Equation (13). This flux can be rewritten as

$$F_{distr}(E) = \frac{c}{4\pi} \frac{J_0}{\sqrt{4\pi b_0 D_0}} I_{\frac{E}{M}} E^{-n-(\delta+1)/2} \quad (29)$$

where

$$I_{\frac{E}{M}} = \int_1^\infty dx \sqrt{\frac{1-\delta}{1-x^{\delta-1}}} x^{-n} e^{-\frac{E}{M}x} \quad (30)$$

The corresponding flux is shown in Figure 3. Where we compare it with the flux from pulsars listed in the ATNF catalog [28]. We take into account all pulsars with ages $t > 15$ kyr and use the delta-function approximation from Section II. The choice of the lower cutoff, 15 kyr, on the age of the pulsars is motivated by the fact that young pulsars, such as the Vela pulsar, usually have a Pulsar Wind Nebula and the electrons haven't yet escaped to the ISM.

In the calculation of the flux from ATNF pulsars, we use the following parameters: injection spectrum

cutoff $M = 10$ TeV, index $n = 1.5$, conversion efficiency $\eta = 0.1$. In order to estimate the initial rotational energy, we assume the average pulsar time scale $\tau = 1$ kyr. Then we use Equation (B6) to express the initial rotational energy, $\mathcal{E}_0 \equiv W_0$, in terms of the current spin down luminosity $\dot{\mathcal{E}}$ and the pulsar age $t \gg \tau$

$$W_0 \approx \dot{\mathcal{E}} \frac{t^2}{\tau} \quad (31)$$

The relative normalization of the curves in Figure 3 depends on the pulsar birth rate N_b , or, to be more precise, on the local density of the birth rate. In order to have a good agreement between the two curves for energies 30 – 300 GeV, we require $N_b \approx 1.8 \text{ kyr}^{-1}$, assuming a Milky Way radius $R_{Gal} = 20$ kpc [26] (our calculation fixes the local density of the birth rate. If we assume $R_{Gal} = 14$ kpc, then we need to take $N_b \approx \frac{1.8}{2} \text{ kyr}^{-1}$ in order to achieve the same local density etc).

Below 30 GeV, the main contribution to e^+e^- flux comes from the pulsars with age $t > 10$ Myr. These pulsars typically have a very low spin-down luminosity and are hard to observe: in the ATNF catalog there is a significant drop in the number of pulsars with the spin down luminosities $\dot{E} < 10^{31}$ erg.

B. Statistical cutoff

As one can see in Figure 3, the flux from the continuous distribution grows until a break at $E \sim M = 10$ TeV whereas the flux from the ATNF pulsars has a cutoff at 2 TeV. This discrepancy is due to the rare events when a young pulsar is very close to the observer. On average such pulsars give a big contribution at high energies, but, in a particular collection, there may be no such pulsars.

Since the electrons cool down during propagation, the electrons with high energies come from young pulsars and the cutoff is determined by the age of the youngest pulsar sufficiently close to the observer so that the electrons have time to diffuse through the ISM. We will call the average such cutoff a statistical cutoff.

To estimate the statistical cutoff, we consider a collection of pulsars and choose an observation point. The

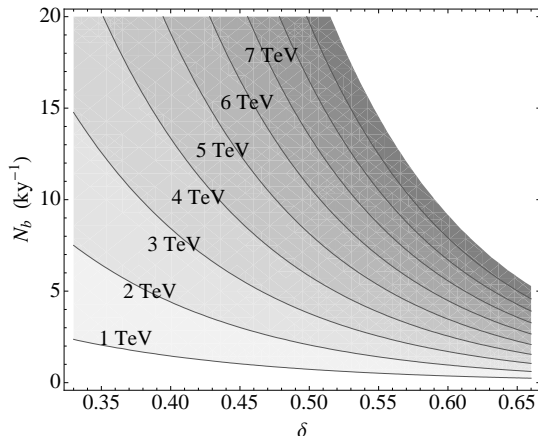


FIG. 4: Statistical cutoff as a function of the diffusion index and the birth rate of pulsars in the galaxy. The cutoff in e^+e^- flux from pulsars is determined by the age of the youngest pulsar within the diffusion distance from the Earth. The average such cutoff is a universal quantity that depends on the properties of ISM (the energy losses and the diffusion coefficient) and on the pulsar birth rate, but it is insensitive to the properties of the injection spectrum from the pulsars. We assume $D_0 = 100 \text{ pc}^2 \text{ kyr}^{-1}$ and $b_0 = 5 \cdot 10^{-6} \text{ GeV}^{-1} \text{ kyr}^{-1}$.

statistical cutoff at this point is the maximal cooling break energy for the flux from these pulsars. Consider the youngest pulsar such that its electrons can reach the observation point and denote the age of this pulsar by T and its diffusion distance by R .

For a given pulsar birth rate N_b , the statistical cutoff M_{stat} can be estimated by demanding that there is at least one pulsar within R and younger than T . Therefore, we have a system of three equations for the three unknowns R , T and M_{stat} :

$$M_{stat} = \frac{1}{b_0 T} \quad (32)$$

$$R^2 = 4D(M_{stat})T \quad (33)$$

$$N_b T \frac{\pi R^2}{A_{Gal}} = 1 \quad (34)$$

Solving this system of equations, we find

$$M_{stat} = \left(\frac{4\pi D_0 N_b}{b_0^2 A_{Gal}} \right)^{\frac{1}{2-\delta}} \quad (35)$$

Assuming $R_{Gal} = 20 \text{ kpc}$, $D_0 = 10^{-4} \text{ kpc}^2 \text{ kyr}^{-1}$, and

$b_0 = 5 \times 10^{-6} \text{ GeV}^{-1} \text{ kyr}^{-1}$, we get

$$M_{stat} = (4 \times 10^5 N_b)^{\frac{1}{2-\delta}} \text{ GeV} \quad (36)$$

where N_b is in units of kyr^{-1} . The statistical cutoff as a function of N_b and the diffusion index δ is shown in Figure 4. This calculation should be viewed as an order of magnitude estimation. Any distribution of real pulsars can have a significant deviation from the average statistical cutoff. For instance, there is little observational data above 2 TeV and it is possible that some future experiment will detect an increase in $E^3 F(E)$ in multi-TeV energies due to electrons from the Vela pulsar [14]. Vela pulsar has a Pulsar Wind Nebula and we assume that most of its electrons are still trapped in the nebula's magnetic fields.

The continuous distribution flux (29) with the statistical cutoff $M_{stat} = 2 \text{ TeV}$ is plotted in Figure 8. The corresponding fit parameters can be found from (29)

$$f_a = \frac{c}{4\pi} \frac{J_0}{\sqrt{4\pi b_0 D_0}} I_{\frac{E_0}{M}} I_{\frac{E_0}{M}}^{3-n-(\delta+1)/2} \quad (37)$$

$$n_a = n + \frac{1+\delta}{2} \quad (38)$$

where $I_{\frac{E_0}{M}} = 2.7$ for $E_0 = 100 \text{ GeV}$ and $M = 10 \text{ TeV}$. In Figure 8 we use $n = 1.5$, $\delta = 0.4$, the birth rate $N_b = 1.8 \text{ kyr}^{-1}$, and the efficiency of conversion $\eta = 0.09$. All other parameters are as usual $W_0 = 10^{50} \text{ erg}$, $D_0 = 10^{-4} \text{ kpc}^2 \text{ kyr}^{-1}$, and $b_0 = 5 \cdot 10^{-6} \text{ GeV}^{-1} \text{ kyr}^{-1}$.

C. Fluctuations around continuous distribution flux

As discussed above, a characteristic feature of the flux from a collection of pulsars is the presence of fluctuations around a smooth curve at high energies. The value of the fluctuations depends on a few factors. Firstly, pulsars are born at random places within the Galactic plane and have a random age. For a given birth rate, the randomness in the position and in age provides the minimal amount of fluctuations. Secondly, there are fluctuations in the flux due to randomness in the initial rotational energy.

The theoretical estimation of fluctuations is rather involved and not very descriptive. Instead, we will describe the characteristic properties of the flux for a few

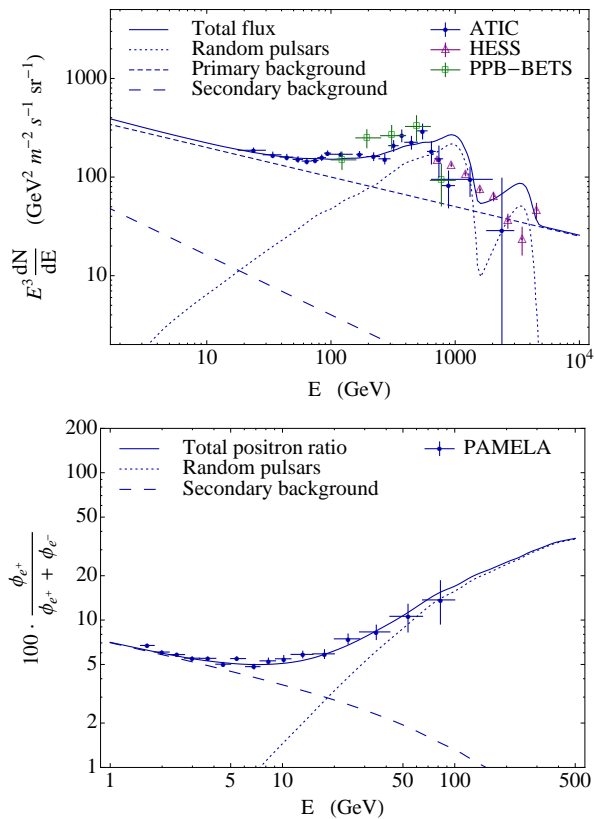


FIG. 5: Flux from randomly generated pulsars. The pulsars have random positions in the Galactic plane and random ages with the average birth rate $N_b = 1.8 \text{ kyr}^{-1}$. We use the delta-function approximation (16) of the pulsar source functions. The mean initial rotational energy is $W_0 = 10^{50}$ erg. The relative standard deviation of W_0 is $\frac{\sigma(W_0)}{W_0} = 0$ in this plot.

collections of randomly generated pulsars. We use the same parameters as the ones listed after formula (38). The pulsars are generated at random position within the Galactic plane and with random age so that the average birth rate is $N_b = 1.8 \text{ kyr}^{-1}$.

The only parameter that hasn't been fixed is the deviation in the initial rotational energy. In the plots, we assume the mean rotational energy $W_0 = 10^{50}$ erg and vary the relative standard deviation $\frac{\sigma(W_0)}{W_0}$. In representing the fluxes, we also apply the smoothing of the peaks due to the spacial variations in the energy losses discussed in Appendix C.

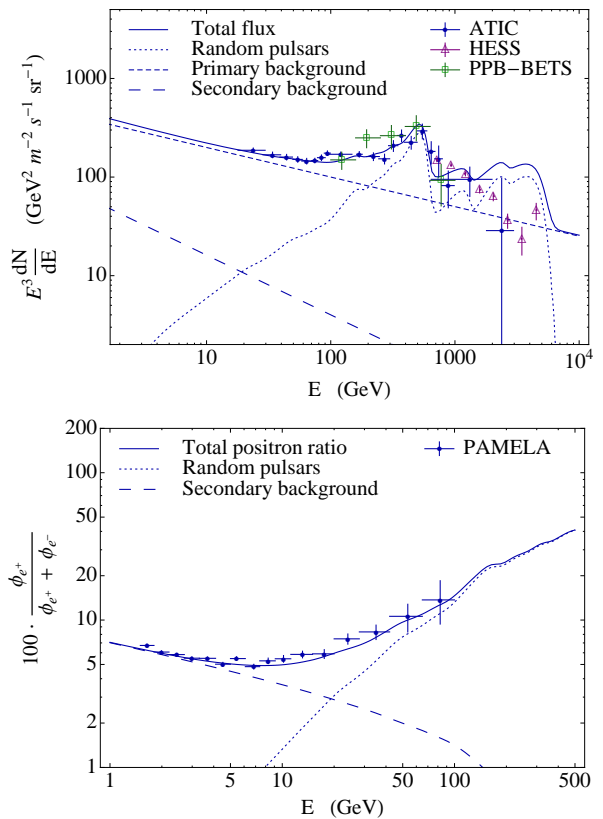


FIG. 6: The same as in Figure 5 but with $\frac{\sigma(W_0)}{W_0} = 3.5$.

The flux with $\frac{\sigma(W_0)}{W_0} = 0$ has the minimal fluctuations which are only due to randomness in position and in age of pulsars. In this plot, after the first bump the flux approaches a smooth curve. The plot with $\frac{\sigma(W_0)}{W_0} = 3.5$ has a few bumps above 300 GeV.

If we increase the variation of initial energy to $\frac{\sigma(W_0)}{W_0} = 14$, then there are large fluctuations in the flux even at smaller energies. For example, in Figure 7 the flux from random pulsars decreases above 100 GeV and increases again around 1 TeV.

The fluxes from random pulsars in Figures 5, 6, and 7 have a cutoff at similar values, 2 - 5 TeV. For $N_b = 1.8 \text{ kyr}^{-1}$ and $\delta = 0.4$ we find from Figure 4 that the statistical cutoff should be $M_{stat} \approx 1 \text{ TeV}$ (which is a reasonable order of magnitude estimation).

The positron ratio in Figures 5 and 6 increases up to a few hundred GeV but in Figure 7, due to large

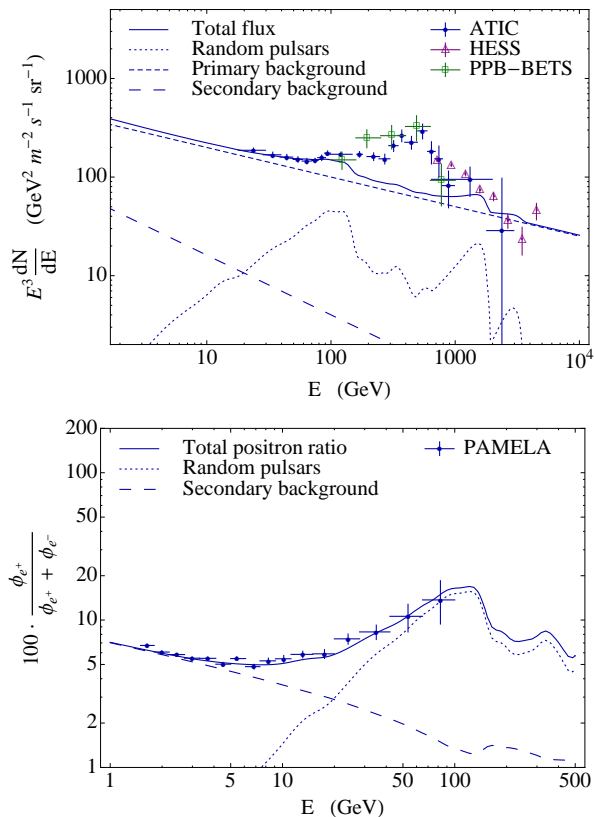


FIG. 7: The same as in Figure 5 but with $\frac{\sigma(W_0)}{W_0} = 14$.

fluctuations in the initial rotational energy, the ratio drops after 100 GeV. The total flux of electrons and positrons drops in this case as well, i.e. it is not compatible with the ATIC bump. If we suppose that the ATIC bump is not confirmed and PAMELA observes no further increase in positron ratio (or even finds a drop after 100 GeV), then this scenario is still compatible with pulsars that have a cutoff in the flux around 1 TeV. However, we would need to assume large fluctuations in the initial rotational energies.

IV. FLUX FROM DARK MATTER

In this section we briefly review the dark matter story and derive that, for a large class of DM models, at energies $E \ll M_{DM}$ the flux has the form of a power law with a universal index $n_a = 2$.

If we neglect the gradients in the DM density near the Earth, then we can use the constant homogeneous source in Equation (9) which gives

$$\rho(E) = \frac{1}{b(E)} \int_E^\infty Q(E') dE' \quad (39)$$

This equation has an interesting property that for any $Q(E) \sim E^k$ with $k > -1$ the integral is saturated at the upper limit which is set by the DM mass M_{DM} . For energies $E \ll M_{DM}$ we can neglect the dependence on E coming from the lower limit of integration and the index of the electron flux is completely determined by the index of the energy loss function $b(E) \sim E^2$.

The source function of e^+e^- coming from annihilating Dark Matter is

$$Q(E) = \frac{1}{2} n_\chi^2 \langle \sigma v \rangle \frac{dN}{dE} \quad (40)$$

where n_χ is the dark matter number density, $\langle \sigma v \rangle$ is the thermally averaged annihilation cross-section, and dN/dE is the number density of electrons and positrons produced per annihilation event. Here we assume that the DM particle is a Majorana fermion, i.e., the particle is its own antiparticle. For a Dirac fermion we would have an extra factor of $\frac{1}{2}$ in (40).

The flux of electrons and positrons from annihilating DM is

$$F(E) = \frac{c}{8\pi} \frac{1}{b(E)} n_\chi^2 \langle \sigma v \rangle \int_E^M \frac{dN}{dE'}(E') dE' \quad (41)$$

Now we can state the condition for the universal behavior of the DM flux, $F \sim E^{-2}$: the corresponding number density of e^+e^- produced in annihilation of the DM should have an index $k > -1$

$$\frac{dN}{dE} \sim E^k \quad k > -1. \quad (42)$$

There are many dark matter models in this class, for instance, the models with a new light force carrier [5][9] or Kaluza-Klein dark matter models [29][30][31]. The main requirement is that there are not more than about three steps in the decay of DM particles into e^+e^- , otherwise the injection spectrum of e^+e^- becomes too steep and condition (42) is violated. In these models, the integral on the right hand side of Equation (41) can

be approximated by the constant

$$I_{e^\pm} = \int_0^M \frac{dN}{dE}(E') dE' \quad (43)$$

which is the average total number of electrons and positrons produced in an annihilation event.

Dark matter with the current energy density $\rho_\chi = 0.3 \text{ GeVcm}^{-3}$ requires $\langle\sigma v\rangle_0 = 3.0 \times 10^{-26} \text{ cm}^3\text{s}^{-1}$ at freeze out. One can assume that the current cross section is larger by a boost factor, BF. We will take the mass of the DM particles $M_{DM} \sim 1 \text{ TeV}$.

The fit parameters n_a and f_a for the dark matter are

$$n_a = 2 \quad (44)$$

$$f_a = \frac{c}{8\pi} \frac{E_0^3}{b(E_0)} n_\chi^2 \langle\sigma v\rangle_0 I_{e^\pm} \cdot BF \quad (45)$$

where as usual we normalize the flux at $E_0 = 100 \text{ GeV}$.

For the DM model [9] with the annihilation chain, $\chi + \chi \rightarrow \phi + \phi \rightarrow 2e^+ + 2e^-$, the f_a parameter (2) is obtained with

$$BF \sim 500. \quad (46)$$

We use this model in Figure 8.

For decaying DM, Equation (41) is replaced by

$$F(E) = \frac{c}{4\pi} \frac{1}{b(E)} \frac{n_\chi}{\tau_d} \int_E^M \frac{dN}{dE'} dE'. \quad (47)$$

where τ_d is the life-time of the DM particle and $\int \frac{dN}{dE} dE$ is the number of electrons and positrons produced per decay. If we take the same number density and the mass of DM particles as above, then

$$\frac{I}{\tau_d} \sim 5 \times 10^{-27} \text{ s}^{-1}. \quad (48)$$

These estimates agree with the analysis of [17] [32] [33].

V. CONCLUSIONS AND OUTLOOK

Anticipating new results from the observations of high energy electrons and positrons in cosmic rays, we would like to discuss the possible predictions and their interpretation in terms of pulsars and dark matter.

One of the main problems in interpreting the results of the experiments is model dependence. In Figure 8

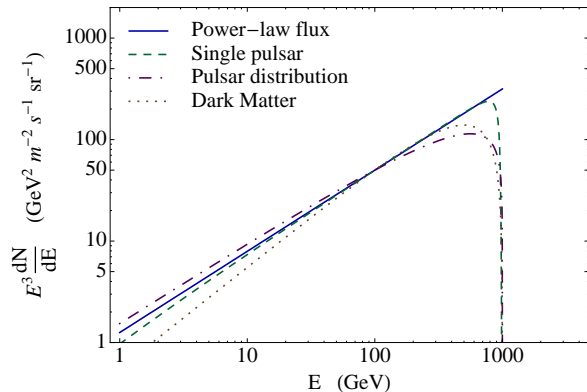


FIG. 8: The fluxes from annihilating dark matter, from a single pulsar, and from a continuous distribution of pulsars can be made similar, depending on the parameters of the models. These fluxes were derived in Sections II, III, and IV.

we show the fluxes from a single pulsar, from a continuous distribution of pulsars, and from a dark matter model. We choose the parameters such that the fluxes at 100 GeV are the same, the indices are close to the best fit value $n_a = 2.2$, and the cutoffs are at 1 TeV. The fluxes from a single pulsar, from a continuous distribution of pulsars, and from dark matter were derived in Sections II, III, and IV respectively. Given the significant uncertainties in the pulsar and DM models, we find it rather improbable that even better observations can distinguish between a single pulsar and dark matter [34].

As we discussed earlier, a model independent signature of pulsars is the presence of bumps or steps in e^+e^- flux at high energies. In Figure 9 we show a possible outcome of the Fermi/GLAST (FGST) experiment after 1 year of observations. In this example, there are two distinctive steps between 300 GeV and 1 TeV. Below 300 GeV the flux is well approximated by a power law. Unfortunately FGST has an effective cutoff around 1TeV in the observation of electrons and most probably we will not see the last bump due to the youngest pulsar within the reach of the Earth. But we believe that FGST should be able to resolve the smaller bumps/steps between 100 GeV and 1 TeV.

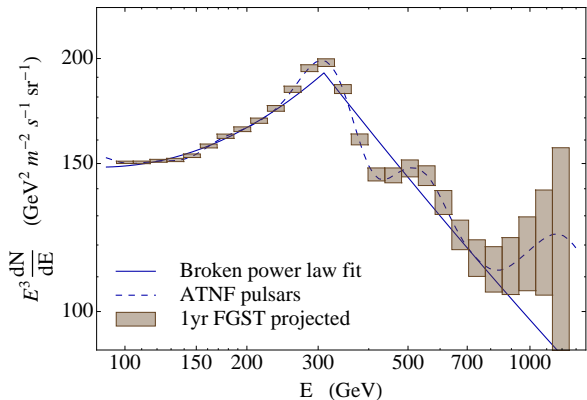


FIG. 9: An e^+e^- flux that may be observed by Fermi/GLAST (FGST) after one year of observations (see text for the discussion of assumptions and parameters). The model independent signature of pulsars is the presence of the steps in the flux. The position and the shape of the steps is model dependent and may be different in the actual data.

The data points in Figure 9 are derived as follows. We take the flux from the ATNF catalog pulsars derived in Section III and apply the Gaussian smearing due to the variations in energy losses (discussed in Appendix C) and due to the energy resolution of FGST (the energy resolution is modeled with the linear function equal to 5% at 20 GeV and 20% at 1 TeV [35]). In this example we take the 1.1 binning, i.e. $E_{i+1} = 1.1E_i$, and calculate the expected number of events in every bin using total flux (backgrounds + pulsars) multiplied by the geometric factor [35] (effective telescope area) and the observation time

$$N_i = T_{observe} \int_{E_i}^{E_{i+1}} F_{tot}(E) \cdot GF(E) dE \quad (49)$$

The error bars in Figure 9 are the statistical errors $\sqrt{N_i}$. The points and the error bars in the plot are rescaled by $E_{(i)}^3$, where $E_{(i)} = \sqrt{1.1}E_i$ is the energy in the center of the bins.

A. A roadmap for possible outcomes of cosmic rays experiments

Let us summarize a few possibilities for the results of high energy cosmic ray experiments and their interpretation in terms of pulsars and DM. In general, scenarios with non-trivial features should correspond to pulsars, whereas feature-less scenarios point to dark matter.

In the following we will write “ATIC +” (“ATIC –”) if the ATIC bump is confirmed (not confirmed), “PAMELA \nearrow ” (“PAMELA \searrow ”) if the PAMELA positron ratio continues to rise until 300 GeV (the positron ratio shows a break above 100 GeV).

Possible scenarios with features are:

- PAMELA \nearrow , ATIC + and there are a few bumps or steps before the ATIC cutoff. This scenario may be observed by Fermi/GLAST as in Figure 9.
- PAMELA \searrow , ATIC +. Since PAMELA will measure the positron ratio only up to 300 GeV, it is possible that, in analogy with Figure 7, there is an older energetic pulsar responsible for the current PAMELA signal and a younger energetic pulsar responsible for the ATIC bump.
- PAMELA \searrow or \nearrow , ATIC –, but there is another bump above 1 TeV. This example is the same as the previous one, but the younger pulsar gives a bump in the flux outside the ATIC energy range.

Scenarios without features assume that there are no significant bumps or steps in e^+e^- flux or positron ratio for any energies. Then dark matter is more probable than pulsars, and, depending on the remaining combinations of observational results, one can constrain the DM mass:

- PAMELA \nearrow , ATIC +, then M_{DM} is found from the break in the ATIC data.
- PAMELA \nearrow , ATIC –, then $M_{DM} \sim 300$ GeV.
- PAMELA \searrow , ATIC –, then M_{DM} is found from the break in the PAMELA data.

The above possibilities represent the boundary cases. In general, one can consider more complicated scenarios, when both dark matter and pulsars give comparable contributions, or dominate at different energies. Also it is possible that there are several species of dark matter particles with different masses that mimic the pulsar flux. In order to separate these scenarios one will need an independent method, such as the observation of the diffuse gamma rays from the center of the Galaxy [19].

Acknowledgments.

The authors are thankful to Gregory Gabadadze, Andrei Gruzinov, Ignacy Sawicki, Jonathan Roberts, and Alex Vikman for valuable discussions. We are especially indebted to Neal Weiner for initiating the project and for numerous discussions and support during all stages of the work. This work is supported in part by the Russian Foundation of Basic Research under grant RFBR 09-02-00253 (DM), by the NSF grants PHY-0245068 (DM) and PHY-0758032 (DM), by DOE OJI grant DE-FG02-06E R41417 (IC), by the NSF Astronomy and Astrophysics Postdoctoral Fellowship under award AST-0702957 (JG).

APPENDIX A: ELECTRON AND POSITRON BACKGROUNDS

In this appendix we discuss the electron and positron backgrounds. The background fluxes consist of primary electrons and secondary electrons and positrons. Primary electrons come from “relic” particles that were recently accelerated via some mechanism, e.g., Fermi acceleration [23]. We assume that there are no primary positrons, as we consider their contribution to the overall positron background flux to be small. Secondary electrons and positrons are produced in collisions of high energy cosmic ray protons and nuclei with the low energy protons and nuclei. Due to the charge conservation and CP invariance, these processes result in an equal flux of secondary electrons and positrons.

In Figure 1 we approximate the backgrounds with power laws and find the best fit to the low energy ATIC and PAMELA points

$$E^3 \frac{dN_i}{dE} = f_i \left(\frac{E}{E_0} \right)^{3-n_i} \quad (\text{A1})$$

where $i = p$ for primary background and $i = s$ for secondary background. The best fit values are

$$\begin{aligned} f_p &= 100 \text{ GeV}^2 \text{ m}^{-2} \text{ s}^{-1} \text{ sr}^{-1} & n_p &= 3.3 \\ f_s &= 4 \text{ GeV}^2 \text{ m}^{-2} \text{ s}^{-1} \text{ sr}^{-1} & n_s &= 3.6 \end{aligned}$$

In the energy range 10 GeV – 1 TeV, these backgrounds agree with [36] and with the gamma-ray and synchrotron studies [21].

It may seem that our approach oversimplifies the problem, since the PAMELA points below 10 GeV are affected by the solar modulation and the background spectral indices vary with the energy. However, the additional source dominates at energies above 10 GeV and, as a result, its properties are robust with respect to the small variations of the backgrounds at low energies.

As an example of the background independence we take the backgrounds that agree with the local CR spectra as well as the gamma-ray and synchrotron studies [21]. These backgrounds can be found from [36]. A corresponding fit is shown in Figure 10. The best fit values for the normalization f_a and the index n_a of the

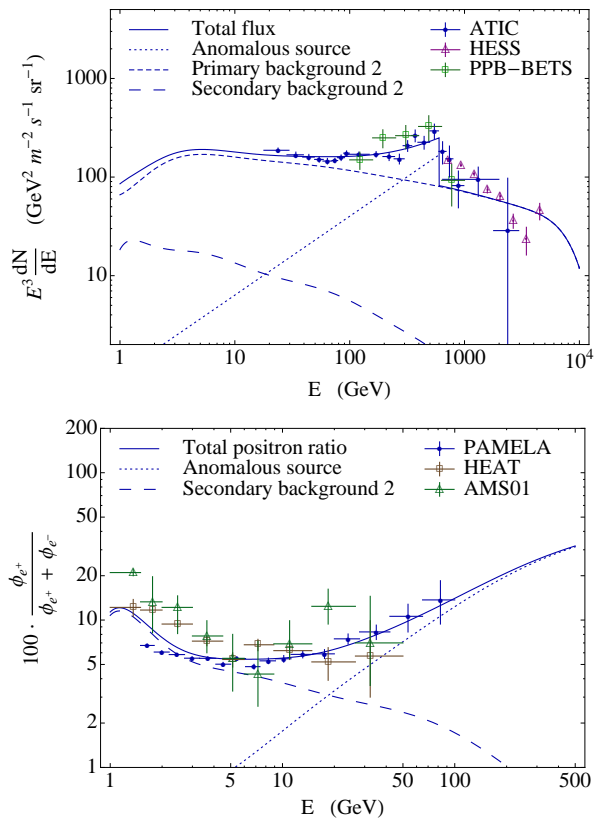


FIG. 10: Power law fit to the ATIC and PAMELA data with a conventional background model [36]. The fit parameters of the additional flux are given in formula (A2). They show good agreement with the fit parameters in formula (2) derived for simple power law backgrounds shown in Figure 1.

additional flux are

$$\begin{aligned} f_a &= (40 \pm 10) \text{ GeV}^2 \text{ m}^{-2} \text{ s}^{-1} \text{ sr}^{-1} \\ n_a &= 2.2 \pm 0.2 \end{aligned} \quad (\text{A2})$$

in good agreement with the values found in formula (2).

APPENDIX B: REVIEW OF PULSARS

In this appendix we review the emission of electrons from pulsars. The main goal is to motivate the source

function

$$Q(\mathbf{x}, E, t) = Q(E) \frac{1}{\tau} \left(1 + \frac{t}{\tau}\right)^{-2} \delta(\mathbf{x}), \quad (\text{B1})$$

where

$$Q(E) = Q_0 E^{-n} e^{-E/M} \quad (\text{B2})$$

and find a reasonable range of parameters for Q_0 , n , M and τ .

Pulsars are believed to be rotating neutron stars with a strong surface magnetic field [25]. The magnetic dipole radiation is a good approximation to describe the energy loss mechanism. The gravitational radiation may contribute to the energy losses but it has been shown in some cases to dominate only in the first ~ 100 yr of the pulsars life [25]. The characteristic decay time τ is defined as

$$\tau = \frac{\mathcal{E}_0}{\dot{\mathcal{E}}_0}, \quad (\text{B3})$$

where \mathcal{E}_0 and $\dot{\mathcal{E}}_0$ are the initial rotational energy and the initial spin down luminosity

$$\begin{aligned} \mathcal{E}_0 &= \frac{1}{2} I \Omega_0^2 \\ \dot{\mathcal{E}}_0 &= \frac{B_p^2 R^6 \sin^2 \alpha}{6c^3} \Omega_0^4 \end{aligned}$$

where Ω_0 is the initial angular velocity, R is the radius of the pulsar, B_p is the surface magnetic field, α is the angle between the rotation axis and the magnetic field axis.

The energy loss due to magnetic dipole radiation is

$$I \Omega \dot{\Omega} = - \frac{B_p^2 R^6 \sin^2 \alpha}{6c^3} \Omega^4 \quad (\text{B4})$$

Integrating the energy loss equation we get

$$\Omega(t) = \Omega_0 \left(1 + \frac{t}{\tau}\right)^{-\frac{1}{2}}, \quad (\text{B5})$$

$$\dot{\mathcal{E}}(t) = \mathcal{E}_0 \frac{1}{\tau} \left(1 + \frac{t}{\tau}\right)^{-2}. \quad (\text{B6})$$

As a result, the pulsar period satisfies

$$\frac{P}{2\dot{P}} = - \frac{\Omega}{2\dot{\Omega}} = t + \tau \quad (\text{B7})$$

As an example, let us calculate the initial rotational energy of the Crab pulsar. The current observations for the period and the period derivative are $P = 0.033$ s and $\dot{P} = 4.2 \times 10^{-13}$ s/s [37][28], thus $P/2\dot{P} = 1.24$ kyr. The Crab pulsar is believed to have been produced during SN 1054 supernova explosion. Consequently the age is $t = 955$ yr and the pulsar time scale is $\tau \approx 0.3$ kyr. Assuming the pulsar mass $1.4 M_\odot$, radius $R = 12$ km, and moment of inertia $I = 1.4 \times 10^{45}$ g cm² [25], we derive $\Omega_0 \approx 600$ s⁻¹ and the initial energy $W_0 \approx 3 \times 10^{50}$ erg.

The Crab pulsar is believed to be significantly more energetic than the average. A typical pulsar is expected to have a much smaller initial energy, $W_0 \sim (10^{48} - 10^{49})$ erg (e.g., Table 7 in [26] contains a list of initial spin periods and references). Although the median energy can be small, the mean initial energy can be big due to a few energetic pulsars. We therefore assume the following mean values

$$W_0 = 10^{50} \text{ erg} \quad (\text{B8})$$

$$\tau = 1 \text{ kyr} \quad (\text{B9})$$

It is also important to understand how the pulsar's magnetic dipole radiation is transferred to the kinetic energy of particles. Since the spin-down luminosity decays as t^{-2} , we are mostly interested in young pulsars. A young pulsar is surrounded by several layers [38][39]. Nearest to the neutron star is a magnetosphere which ends at the light cylinder $R_{LC} = c/\Omega$. The rotating magnetic field creates a strong electric field that is capable of both producing pairs of particles and accelerating them to relativistic energies. These particles stream away from the light cylinder as a coherent “wind” that ends with a termination shock separating the “wind” zone and the Pulsar Wind Nebula (PWN) consisting of magnetic fields and particles moving in random directions. The PWN is surrounded by the supernova remnant (SNR). The PWN and the SNR exist only at the early times $t \ll 100$ kyr.

The spectrum of the electrons and positrons in the magnetosphere can be found from the pulsed γ -ray emission from the pulsar. The spectrum of e^+e^- pairs in the magnetosphere of the Crab pulsar can be fitted by the broken power law with index 2.0 below $E_{br} \sim 2$

GeV and index 2.8 between E_{br} and an upper cutoff around 100 GeV [40] (see also [41]). The cutoff at 100 GeV is too low to explain ATIC and just enough to account for PAMELA.

These particles are further accelerated by the termination shock between the magnetosphere and the Pulsar Wind Nebula (for a review see, e.g., [42]), after which they are trapped by the magnetic field inside the PWN until it is disrupted. Observationally, the spectrum of the electrons inside the PWN is found from their synchrotron radiation and high energy photons created through the inverse Compton scattering off CMB [27].

The best known example is the spectrum of the electrons in the Crab PWN [27]: it has the form of a broken power law with index $n = 1.5$ below $E_0 \sim 200$ GeV and $n = 2.4$ between E_0 and an upper cutoff $E_{cut} \sim 10^3$ TeV. The best fit for the electron spectrum is obtained for a PWN magnetic field $B \approx 2 \times 10^{-4}$ G and a ratio of magnetic energy flux to particle energy flux of $\sigma < 0.01$.

Let us spend a little time on the interpretation of these numbers. The break at E_0 is related to cooling via the synchrotron radiation in the PWN magnetic field

$$\frac{dE}{dt} = -bE^2, \quad b = \frac{2(e^2 B \sin \theta)^2}{3 m^4} \quad (\text{B10})$$

For $B = 2 \times 10^{-4}$ G and the age of the pulsar $t = 1$ kyr this gives $E_{br} \sim 400$ GeV. This is an upper bound on the cooling break energy: as the PWN expands the energy density of the magnetic field decreases. As a result, at earlier times the magnetic field is larger and the synchrotron losses are greater. Electrons with energies below the break are not affected by the synchrotron cooling, and the index $n = 1.5$ reflects the initial injection spectrum from the termination shock acceleration. The upper cutoff $E_c \sim 10^3$ TeV characterizes the maximal electron energies after the termination shock. The small value σ means that the PWN is particle dominated and more than 99% of the energy is in the particle wind.

Some comments about the cooling break and the efficiency of conversion are in order:

- The current cooling break for the Crab PWN is

200 GeV whereas we assume that the break in the injection from the pulsars is at 10 TeV. The reason is that the magnetic field in the PWN decreases with time and electrons emitted at later times lose less energy, pushing the energy cutoff higher. We assume that by the time the PWN disappears, the cooling break has increased up to a few TeV. This reasoning is supported by observations of the Vela PWN. The Vela pulsar is 10 times older than the Crab pulsar, the magnetic field in Vela PWN is estimated to be 10^{-5} G, which gives the characteristic cooling break energy $E_{br} = 16$ TeV. This agrees also with an observed break in the spectrum of Vela TeV photons at 13 TeV [43]. We are not aware of an analysis of the corresponding break in the Vela electrons but we expect it to be on the same order of magnitude. In fact, the exact value of the break is not important as far as it is bigger than ≈ 1 TeV.

- Observations indicate that most PWN are particle dominated, i.e. almost 100% of the spin-down luminosity is transformed into the energy of the particles after the termination shock. Let us explain why then, the eventual conversion efficiency into electron-positron pairs $\eta \lesssim 10\%$. Assume that the spectrum after the termination shock is a power law $Q(E) \sim E^{-n}$ with an index $n < 2$ and a cutoff $E_c \sim 10^3$ TeV. Then, the total energy in electrons is

$$W_{ini} \sim \int E^{-n} E dE \sim E_c^{2-n}. \quad (\text{B11})$$

Suppose that at the time of PWN disruption the energy spectrum is E^{-n} before the break at E_{br} and E^{-n_b} with $n_b > 2$ after the break. Then the total energy in electrons is saturated at E_{br} with

$$W_{fin} \sim E_{br}^{2-n}. \quad (\text{B12})$$

The efficiency is therefore

$$\eta = \frac{W_{ini}}{W_{fin}} \sim \left(\frac{E_{br}}{E_c} \right)^{2-n} \quad (\text{B13})$$

For $n = 1.5$, $E_{br} = 10$ TeV and $E_c = 10^3$ TeV, this gives the suggested $\eta = 0.1$. This deriva-

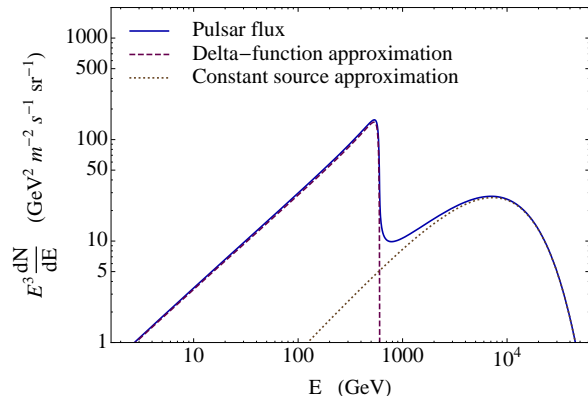


FIG. 11: The flux from Geminga pulsar. The delta-function approximation works well below the cooling break at 600 GeV. The constant source approximation provides a good approximation above the cooling break. The flux decreases by an order of magnitude across the cooling break.

tion should be viewed as an order of magnitude estimation. A more realistic calculation is much more complicated and involves the knowledge of the PWN evolution and the actual spectra of particles inside a PWN.

It should be stressed that, apart from theoretical uncertainties, the parameters of the injection spectrum can vary significantly for different pulsars. The initial rotational energy can differ by several orders of magnitude, while the index of the electron spectrum n can vary from 1 to 2. In some cases, it is observed to vary inside the Pulsar Wind Nebula of a single pulsar. The upper cutoff M can be up to an order of magnitude different from 10 TeV.

This variation between the pulsars is a distinctive feature that will cause some “random” fluctuations of the flux around an average curve. As we discuss in this paper, a model independent way to distinguish between a pulsar and a Dark Matter origin for the PAMELA and ATIC e^\pm excess is to look at fluctuations in the energy spectrum. A smooth curve with a single cutoff is expected for Dark Matter or a single pulsar, but a spectrum that has significant fluctuations around an average curve corresponds to the contribution from a collection of pulsars.

In order to summarize our discussion of e^+e^- flux from pulsars, we present the flux from Geminga pulsar in Figure 11. We use the parameters $\tau = 1$ kyr, $M = 10$ TeV, $n = 1.6$, and $\eta = 0.1$. We compare this flux with the delta-function approximation, $\tau \rightarrow 0$, that we use in this paper. In the constant source approximation we assume that the pulsar is a constant source with the current spin-down luminosity.

APPENDIX C: SMOOTHING DUE TO SPATIAL VARIATION IN ENERGY LOSSES

As we have discussed an important signature of the flux from the pulsars is the presence of a number of bumps at the cooling break energies

$$E_i = \frac{1}{bt_i} \quad (\text{C1})$$

where t_i 's are the ages of the pulsars. The existence of the bumps is based on the assumption that the energy losses only depend on the time traveled by the particles and don't depend on the paths.

In reality, the energy loss coefficient depends on the coordinates, since the densities of the star light and IR photons vary in space. Although Equation (9) with $b(E, x)$ doesn't have a simple solution, one can still find the average energy loss and its standard deviation by averaging the energy losses over the random paths.

As a useful simplification we will consider separately the diffusion in space and the energy losses. The motivation is that a particle detected with the energy E most of the time has its energy close to E (i.e. the cooling time from E_0 to E is saturated by the final energy E). Consequently, the diffusion coefficient for all the particles detected with the energy E can be approximated by $D(E)$.

Then the probability to propagate from a source at (x_0, t_0) to an observer at (x_1, t_1) is given by the Green function

$$G(x_1, t_1; x_0, t_0) = \frac{1}{(4\pi D(E)\Delta t)^{3/2}} e^{-\frac{\Delta \mathbf{x}^2}{4D(E)\Delta t}} \quad (\text{C2})$$

In order to find the energy loss averaged over paths, it is useful to rewrite this Green function in terms of the

path integral

$$G(\mathbf{x}_1, t_1; \mathbf{x}_0, t_0) = \int Dx(t) e^{-S[x(t)]} \quad (\text{C3})$$

where the action is

$$S[x(t)] = \int \frac{1}{4D(E)} \dot{x}^2 dt \quad (\text{C4})$$

with the boundary conditions $x(t_0) = x_0$ and $x(t_1) = x_1$.

In general, the average of a functional $\mathcal{O}[x(t)]$ over paths is

$$\langle \mathcal{O} \rangle = \frac{\int Dx(t) \mathcal{O}[x(t)] e^{-S[x(t)]}}{\int Dx(t) e^{-S[x(t)]}}. \quad (\text{C5})$$

Integrating the energy loss

$$\frac{dE}{dt} = -b(x)E^2 \quad (\text{C6})$$

along a path $x(t)$, we find

$$\frac{1}{E_1} - \frac{1}{E_0} = \int_{t_0}^{t_1} b(x) dt. \quad (\text{C7})$$

The functional that we will study is

$$\mathcal{O}[x(t)] = \int_{t_0}^{t_1} b(x) dt. \quad (\text{C8})$$

The expression in the numerator of (C5) is

$$\begin{aligned} \text{Numerator} &= \int Dx(t) \int_{t_0}^{t_1} dt' b(x(t')) e^{-S[x(t)]} \\ &= \int_{t_0}^{t_1} dt' \int Dx(t) \\ &\quad \cdot b(x(t')) e^{-S[x(t)]} \end{aligned} \quad (\text{C9})$$

If we define $x' = x(t')$, then all the paths can be represented as a path from x_0 to x' , the integral over all x' and the path from x' to x_1

$$\begin{aligned} \text{Numerator} &= \int_{t_0}^{t_1} dt' \int_{x_0}^{x'} Dx(t) \int dx' \int_{x'}^{x_1} Dx(t) \\ &\quad \cdot b(x(t')) e^{-S[x(t)]} \end{aligned} \quad (\text{C10})$$

$$\begin{aligned} &= \int_{t_0}^{t_1} dt' \int dx' G(x_1, t_1; x', t') \\ &\quad \cdot b(x') G(x', t'; x_0, t_0). \end{aligned} \quad (\text{C11})$$

The resulting expression resembles the first order perturbation theory: there is a propagation from x_0 to x' , insertion of an operator at x' and a propagation from x' to x_1 .

The average energy loss can be estimated with (C11) and the Green function in (C2). Taking $E_0 \rightarrow \infty$ in (C7), we find that the average cooling break energy for a given pulsar is

$$\left\langle \frac{1}{E_{br}} \right\rangle \equiv \langle \mathcal{O} \rangle = \left(\int_{t_0}^{t_1} dt' \int dx' G(x_1, t_1; x', t') b(x') \cdot G(x', t'; x_0, t_0) \right) / G(x_1, t_1; x_0, t_0). \quad (\text{C12})$$

The standard deviation is

$$\sigma_{\mathcal{O}} = \sqrt{\langle \mathcal{O}^2 \rangle - \langle \mathcal{O} \rangle^2} \quad (\text{C13})$$

The average $\langle \mathcal{O}^2 \rangle$ for the functional (C8) can be computed analogously to (C12)

$$\begin{aligned} \langle \mathcal{O}^2 \rangle &= 2 G^{-1}(x_1; x_0) \\ &\int_{t_0}^{t_1} dt' \int dx' \int_{t'}^{t_1} dt'' \int dx'' G(x_1; x'') \\ &\cdot b(x'') G(x''; x') b(x') G(x'; x_0) \end{aligned}$$

where we assume that x' is at t' and x'' is at t'' . The factor of two is the usual $n!$ for the time-ordered path integrals.

The relative standard deviation of the cooling break energy is

$$\frac{\Delta E}{E} = \frac{\sigma_{\mathcal{O}}}{\langle \mathcal{O} \rangle} \quad (\text{C14})$$

Using the energy densities of starlight and IR photons from [44] we find the relative smearing in the energy

$$\frac{\Delta E}{E} \approx 0.053 \cdot \left(\frac{E}{1 \text{ TeV}} \right)^{-1/3} \quad (\text{C15})$$

At 1 TeV the smearing is about 5%, at 100 GeV it is 11% , and 24% at 10 GeV. The flux from the ATNF pulsars with this smearing is shown in Figure 12. At low energies the flux becomes very smooth but at high energies the bumps are still visible. We also notice that at high energies the relative width of the bumps is larger than the ratio in (C15). Thus, even if the experimental energy resolution is about 10 – 15%, we should be able to see the bumps.

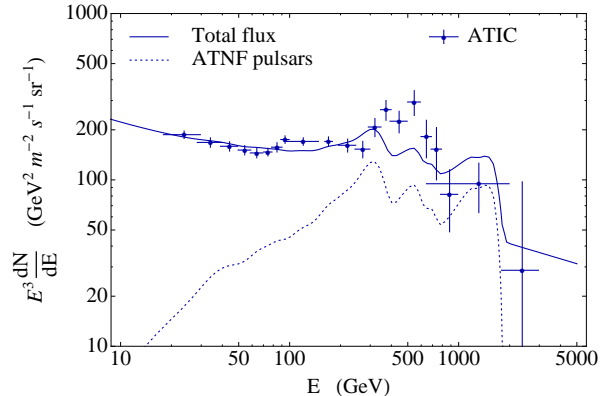


FIG. 12: The flux from the ATNF catalog pulsars [28] with smearing due to spacial variations in the energy losses.

APPENDIX D: CONSTRAINING PROPERTIES OF PULSARS AND ISM

If we assume that the anomalies in ATIC and PAMELA data are due to pulsars, then we can use these experiments to constrain the properties of ISM and pulsars. As we have shown in the introduction, the anomalous flux can be described by a power law function with normalization f_a and index n_a given in equation (2) and a cutoff $E_{cut} > 600$ GeV.

The problem is that the flux depends on both the properties of ISM and the properties of the injection spectrum from pulsars. As we discuss in sections II and III, the ISM properties can be described by three parameters D_0 , δ , b_0 and the injection from a distribution of pulsars can be described by five parameters W_0 , η , n , M , and N_b . Obviously, the three parameters of the observed flux f_a , n_a , and E_{cut} cannot constrain the eight parameters necessary to describe the ISM and the injection from pulsars, but they can constrain some combinations of parameters. These constrains may be very useful if we combine them with the constrains from the other experiments, such as the observations of protons, heavy nuclei, or diffuse gamma rays.

Another concern is the reliability of constrains coming from the local e^+e^- fluxes. Ideally, we would like to constrain the parameters in the models, but pulsars are random by their nature and there is a possi-

bility that we may only constrain some of the properties of some of the pulsars without getting any information about the general picture. The reason why we think our approach is sensible is the following. At high energies the flux from pulsars will depend significantly on the properties of individual pulsars (and we can use this region to prove that the observed flux is due to pulsars), but at low energies the flux is well approximated by the continuous distribution flux and the properties of individual pulsars don't influence the total flux. Thus we propose to use the intermediate energies $100 \text{ GeV} < E < 500 \text{ GeV}$ as a testing ground to study the general (or averaged) properties of e^+e^- injection from pulsars.

In the following we will fit the continuous distribution flux derived in equation (29) to the ATIC and PAMELA data. In the fits we will substitute the usual pulsar injection cutoff $M \sim 10 \text{ TeV}$ by the propagated (or statistical) cutoff M_{stat} and treat it as a fit parameter. The other fit parameters are $b_0 = (0.5 - 3) \times 10^{-16} \text{ GeV}^{-1} \text{ s}^{-1}$ (these values are based on the energy densities of radiation and magnetic field within few kpc from the Earth), $\delta = (0.3 - 0.6)$ [21]. The injection index $n \approx (1 - 2)$ and the conversion efficiency $\eta \sim (0.01 - 0.3)$ are discussed in Appendix B. In the fits we use $D_0 = 100 \text{ pc}^2 \text{ kyr}^{-1}$, $N_b = 1.8 \text{ kyr}^{-1}$, $W_0 = 10^{50} \text{ erg}$. The best fits are obtained for $M_{stat} = 820 \text{ GeV}$.

We also fitted the flux from the ATNF catalog pulsars within 4 kpc from the Earth, with spin down luminosity $10^{31} \leq \dot{E} \leq 5 \times 10^{36} \text{ ergs}^{-1}$, and age less than 10^8 yr . We provide a table where the regions of 95% CL are given for each one of the parameters. In the table we present results for two different backgrounds (see Appendix A).

In Figure 15 we present the constraints for the various parameters with 68%, 95% and 99% CL, where we vary with respect to a reference set of parameter-values that fit well to the ATIC data. A few comments are in order. First we can see that for any value of the energy loss coefficient b_0 within the region chosen, there is a value of diffusion index δ that can provide a fit within 95% CL. Also a higher value of n suggests a lower value of δ , in agreement with the calculation

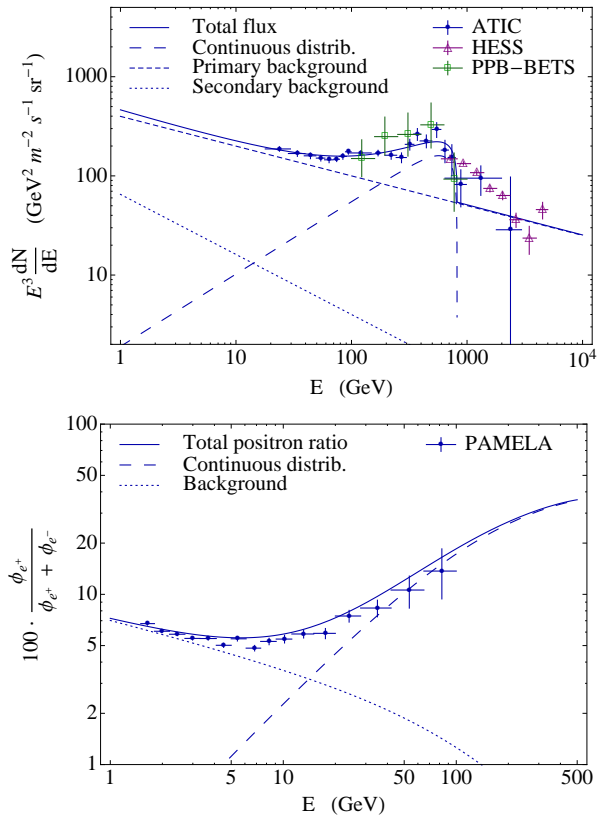


FIG. 13: Electron + positron fluxes and projected positron fraction for the best fit to the ATIC data from a continuous distribution of pulsars.

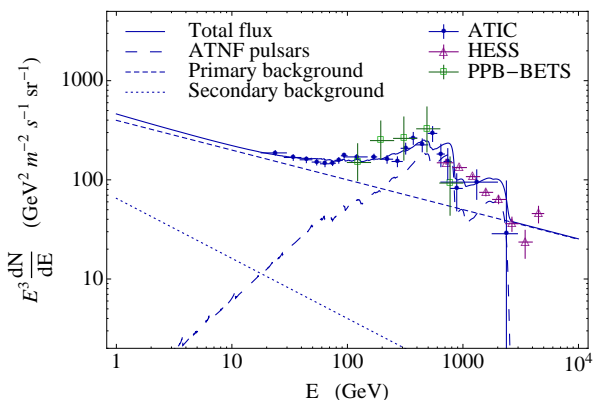


FIG. 14: ATNF pulsars within 4 kpc with changed conversion coefficients η for Geminga, B0656+14 and J0538+2817(see text).

of the flux of e^+e^- , from a continuous distribution of pulsars where we expect that $f_a \propto E^{3-n-(\delta+1)/2}$ from Equation (37). Assuming a high value for the injection index ($n \geq 1.6$), the ATIC data could be fitted by a relatively large region of values of the propagation parameters ($0.3 \leq \delta \leq 0.55$ and $b_0 \leq 3 \times 10^{-16} \text{ GeV}^{-1} \text{ s}^{-1}$). On the other hand, values of $n < 1.0$ don't seem to give a very good fit to the data, with any combination of propagation parameters. Another thing to notice, is that if the total energy converted to e^+e^- , ηW_0 is smaller than $2 \times 10^{48} \text{ erg}$ for a pulsar birth rate of 1.8 per kyr, then regardless of the value of n , the ATIC data can't be explained by the continuous distribution of pulsars. We applied the same analysis to a second background described in **A**. Our results were similar (see table I).

When fitting to the ATNF database pulsars, we expect that pulsars at distances further than 4 kpc will not influence our calculations as their resulting e^+e^- flux having propagated from such distances will influence mainly the region of energies, lower from those of the ATIC data. Our main uncertainty in this calculation comes from relatively young energetic pulsars (such as Geminga) whose flux peaks at the energies of 300 GeV - 1 TeV. As their number is small (of order 10) their actual properties are important. Using observed pulsars in our calculations, the majority of which (but not Geminga) have been discovered in the radio-waveband, we expect that there are pulsars, that contribute to the local e^+e^- flux which we haven't observed, as our line of sight is out of their emission cone (it would be still improbable to have a pulsar source that is as close and energetic as Geminga and still haven't discovered it, in X-rays or γ -rays).

By inspection at Figure 12, we can see that at $E \sim 600 \text{ GeV}$ the flux from the ATNF pulsars is smaller than the ATIC flux. If we assume that Geminga has a conversion coefficient 3 times larger than the rest of the pulsars, while B0656+14 and J0538+2817 a coefficient 2 times smaller, then the ATIC data can be fitted much better (see Figure 14). Those differences in η are easily motivated from the deviations within different pulsars. The fact that we need to increase η of Geminga could mean that either indeed the PWN of Geminga is a very

strong source of e^+ and e^- as indicated by [16] and [15], or that there may be a few missing pulsars contributing at energies $E \sim 600 \text{ GeV}$.

Pulsar Distribution	b_0	δ	n	η
Cont. Dist. B1	0.5-3.0	0.30-0.60	1.05-1.95	0.03-0.32
Cont. Dist. B2	0.5-3.0	0.30-0.60	0.70-1.90	0.03-0.35
4kpc Pulsars B1	0.65-2.05	0.30-0.54	1.20-1.90	0.03-0.13
4kpc Pulsars B2	0.6-2.4	0.30-0.55	1.10-1.90	0.025-0.14

TABLE I: Table of best-fit parameters within 95% CL. In the first two lines, the ranges of b_0 in $10^{-16} \text{ GeV}^{-1} \text{ s}^{-1}$, diffusion index δ , injection index n , and η for a continuous distribution of pulsars are given. We assume that W_0 is 10^{50} erg . In the last two lines the equivalent ranges are given for the distribution of all Pulsars within 4 kpc. B1 and B2 stand for the two backgrounds used.

Better future data on the flux of the high energy e^+e^- and on the birth rate of the pulsars, will make this analysis more successful in confining the parameter space that is relevant for the pulsar scenario. Tighter constraints of the backgrounds and the parameters of propagation through the ISM, will be needed to confine the properties of pulsars themselves.

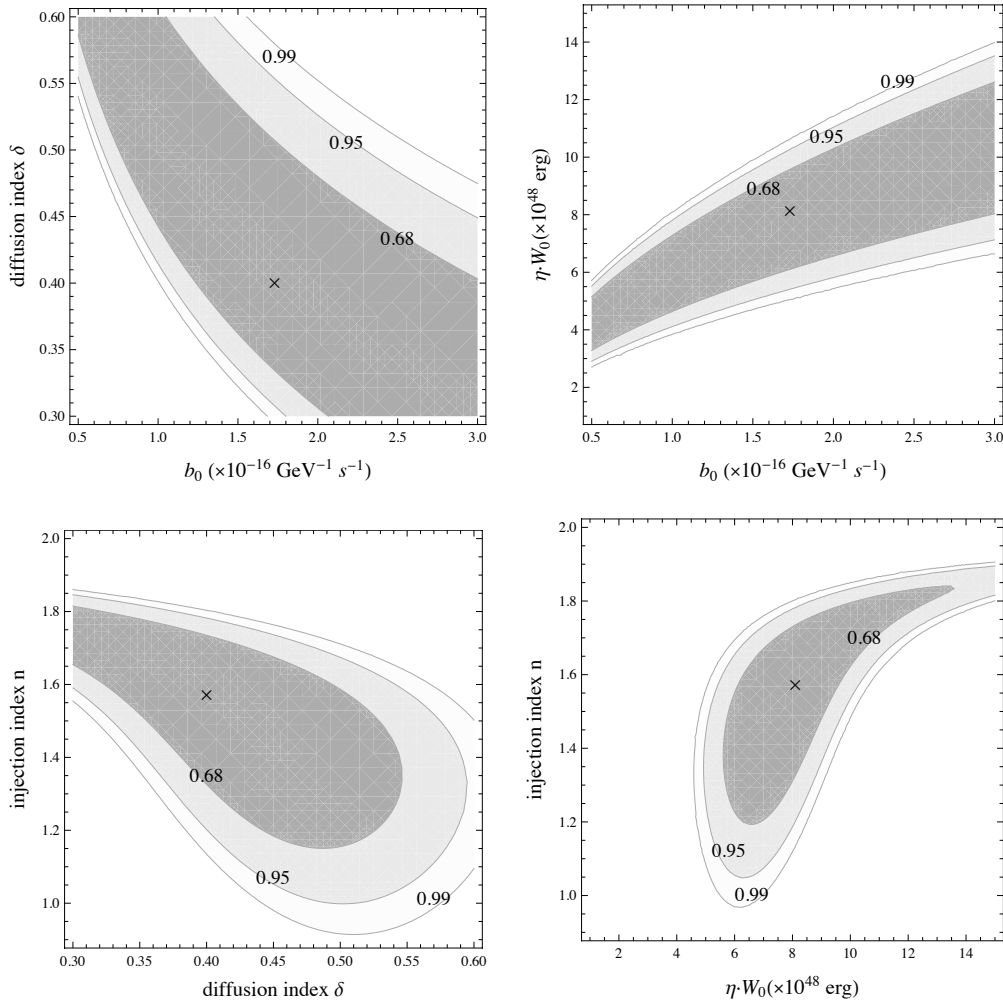


FIG. 15: The fits of the continuous distribution flux to the ATIC and PAMELA data. The best fit parameters are: $\delta = 0.4$, $b_0 = 1.7 \times 10^{-16} \text{ GeV}^{-1} \text{ s}^{-1}$, $\eta W_0 = 8.1 \times 10^{48} \text{ erg}$, $n = 1.57$ and $M_{stat} = 820 \text{ GeV}$. The contours show the confidence levels relative to the best fit, $\sigma^2 = (\chi^2 - \chi_*^2)/dof$, where χ_*^2 is the chi squared for the best fit parameters.

-
- [1] O. Adriani *et al.*, “Observation of an anomalous positron abundance in the cosmic radiation,” [arXiv:0810.4995 \[astro-ph\]](#).
- [2] J. Chang *et al.*, “An excess of cosmic ray electrons at energies of 300.800 GeV,” *Nature* **456** (2008) 362–365.
- [3] S. Torii *et al.*, “High-energy electron observations by PPB-BETS flight in Antarctica,” [arXiv:0809.0760 \[astro-ph\]](#).
- [4] **H.E.S.S.** Collaboration, F. Aharonian *et al.*, “The energy spectrum of cosmic-ray electrons at TeV energies,” *Phys. Rev. Lett.* **101** (2008) 261104, [arXiv:0811.3894 \[astro-ph\]](#).
- [5] I. Cholis, L. Goodenough, and N. Weiner, “High Energy Positrons and the WMAP Haze from Exciting Dark Matter,” [arXiv:0802.2922 \[astro-ph\]](#).
- [6] L. Bergstrom, T. Bringmann, and J. Edsjo, “New Positron Spectral Features from Supersymmetric Dark Matter - a Way to Explain the PAMELA Data?,” *Phys. Rev.* **D77** (2008) 103520, [arXiv:0808.3725 \[astro-ph\]](#).
- [7] M. Cirelli, M. Kadastik, M. Raidal, and A. Strumia, “Model-independent implications of the e^+ , e^- , anti-proton cosmic ray spectra on properties of Dark Matter,” [arXiv:0809.2409 \[hep-ph\]](#).
- [8] I. Cholis, L. Goodenough, D. Hooper, M. Simet, and N. Weiner, “High Energy Positrons From Annihilating Dark Matter,” [arXiv:0809.1683 \[hep-ph\]](#).
- [9] N. Arkani-Hamed, D. P. Finkbeiner, T. Slatyer, and N. Weiner, “A Theory of Dark Matter,” (2008) , [arXiv:0810.0713 \[hep-ph\]](#).
- [10] P.-f. Yin *et al.*, “PAMELA data and leptonically decaying dark matter,” [arXiv:0811.0176 \[hep-ph\]](#).
- [11] K. Hamaguchi, E. Nakamura, S. Shirai, and T. T. Yanagida, “Decaying Dark Matter Baryons in a Composite Messenger Model,” [arXiv:0811.0737 \[hep-ph\]](#).
- [12] C.-R. Chen, K. Hamaguchi, M. M. Nojiri, F. Takahashi, and S. Torii, “Dark Matter Model Selection and the ATIC/PPB-BETS anomaly,” [arXiv:0812.4200 \[astro-ph\]](#).
- [13] F. A. Aharonian, A. M. Atoyan, and H. J. Voelk, “High energy electrons and positrons in cosmic rays as an indicator of the existence of a nearby cosmic tevatron,” *Astron. Astrophys.* **294** (1995) L41–L44.
- [14] T. Kobayashi, Y. Komori, K. Yoshida, and J. Nishimura, “The most likely sources of high energy cosmic-ray electrons in supernova remnants,” *Astrophys. J.* **601** (2004) 340–351, [arXiv:astro-ph/0308470](#).
- [15] D. Hooper, P. Blasi, and P. D. Serpico, “Pulsars as the Sources of High Energy Cosmic Ray Positrons,” *JCAP* **0901** (2009) 025, [arXiv:0810.1527 \[astro-ph\]](#).
- [16] H. Yuksel, M. D. Kistler, and T. Stanev, “TeV Gamma Rays from Geminga and the Origin of the GeV Positron Excess,” [arXiv:0810.2784 \[astro-ph\]](#).
- [17] I. Cholis, G. Dobler, D. P. Finkbeiner, L. Goodenough, and N. Weiner, “The Case for a 700+ GeV WIMP: Cosmic Ray Spectra from ATIC and PAMELA,” [arXiv:0811.3641 \[astro-ph\]](#).
- [18] S. Profumo, “Dissecting Pamela (and ATIC) with Occam’s Razor: existing, well-known Pulsars naturally account for the ‘anomalous’ Cosmic-Ray Electron and Positron Data,” [arXiv:0812.4457 \[astro-ph\]](#).
- [19] J. Zhang *et al.*, “Discriminate different scenarios to account for the PAMELA and ATIC data by synchrotron and IC radiation,” [arXiv:0812.0522 \[astro-ph\]](#).
- [20] **Particle Data Group** Collaboration, C. Amsler *et al.*, “Review of particle physics,” *Phys. Lett.* **B667** (2008) 1.
- [21] A. W. Strong, I. V. Moskalenko, and V. S. Ptuskin, “Cosmic-ray propagation and interactions in the Galaxy,” *Ann. Rev. Nucl. Part. Sci.* **57** (2007) 285–327, [arXiv:astro-ph/0701517](#).
- [22] V. L. Ginzburg and S. I. Syrovatskii, *The Origin of Cosmic Rays*. Pergamon, Oxford, 1964.
- [23] M. S. Longair, *High-energy astrophysics*. Cambridge University Press, 1992.
- [24] S. I. Syrovatskii, “The Distribution of Relativistic Electrons in the Galaxy and the Spectrum of Synchrotron Radio Emission,” *Astr. Zh.* **36** (1959) 17.
- [25] S. L. Shapiro and S. A. Teukolsky, *Black Holes, White Dwarfs, and Neutron Stars*. John Wiley & Sons, 1983.
- [26] C.-A. Faucher-Giguere and V. M. Kaspi, “Birth and Evolution of Isolated Radio Pulsars,” *Astrophys. J.* **643** (2006) 332–355, [arXiv:astro-ph/0512585](#).
- [27] F. A. Aharonian and A. M. Atoyan, “On the mechanisms of gamma radiation in the Crab Nebula,” *Mon. Not. Roy. Astron. Soc.* **278** (1996) 525–541.

- [28] R. N. Manchester, G. B. Hobbs, A. Teoh, and M. Hobbs, “The ATNF Pulsar Catalogue,” [arXiv:astro-ph/0412641](https://arxiv.org/abs/astro-ph/0412641).
<http://www.atnf.csiro.au/research/pulsar/psrcat>.
- [29] G. Servant and T. M. P. Tait, “Is the lightest Kaluza-Klein particle a viable dark matter candidate?,” *Nucl. Phys.* **B650** (2003) 391–419, [arXiv:hep-ph/0206071](https://arxiv.org/abs/hep-ph/0206071).
- [30] H.-C. Cheng, J. L. Feng, and K. T. Matchev, “Kaluza-Klein dark matter,” *Phys. Rev. Lett.* **89** (2002) 211301, [arXiv:hep-ph/0207125](https://arxiv.org/abs/hep-ph/0207125).
- [31] D. Hooper and K. Zurek, “The PAMELA and ATIC Signals From Kaluza-Klein Dark Matter,” [arXiv:0902.0593](https://arxiv.org/abs/0902.0593) [[hep-ph](#)].
- [32] J. Hisano, M. Kawasaki, K. Kohri, and K. Nakayama, “Neutrino Signals from Annihilating/Decaying Dark Matter in the Light of Recent Measurements of Cosmic Ray Electron/Positron Fluxes,” [arXiv:0812.0219](https://arxiv.org/abs/0812.0219) [[hep-ph](#)].
- [33] J. Liu, P.-f. Yin, and S.-h. Zhu, “Prospects for Detecting Neutrino Signals from Annihilating/Decaying Dark Matter to Account for the PAMELA and ATIC results,” [arXiv:0812.0964](https://arxiv.org/abs/0812.0964) [[astro-ph](#)].
- [34] J. Hall and D. Hooper, “Distinguishing Between Dark Matter and Pulsar Origins of the ATIC Electron Spectrum With Atmospheric Cherenkov Telescopes,” [arXiv:0811.3362](https://arxiv.org/abs/0811.3362) [[astro-ph](#)].
- [35] A. A. Moiseev, J. F. Ormes, and I. V. Moskalenko, “Measuring 10-1000 GeV Cosmic Ray Electrons with GLAST/LAT,” [arXiv:0706.0882](https://arxiv.org/abs/0706.0882) [[astro-ph](#)].
- [36] A. A. Abdo *et al.*, “Discovery of TeV gamma-ray emission from the Cygnus region of the galaxy,” *Astrophys. J.* **658** (2007) L33–L36, [arXiv:astro-ph/0611691](https://arxiv.org/abs/astro-ph/0611691).
- [37] A. G. Lyne, R. S. Pritchard, and F. G. Smith, “23 years of Crab pulsar rotational history,” *MNRAS* **265** (1993) 1003–1012.
- [38] M. J. Rees and J. E. Gunn, “The origin of the magnetic field and relativistic particles in the Crab Nebula,” *Mon. Not. Roy. Astron. Soc.* **167** (1974) 1–12.
- [39] C. F. Kennel and F. V. Coroniti, “Confinement of the Crab pulsar’s wind by its supernova remnant,” *Astrophys. J.* **283** (1984) 694.
- [40] A. K. Harding, J. V. Stern, J. Dyks, and M. Frackowiak, “High-Altitude Emission from Pulsar Slot Gaps: The Crab Pulsar,” [arXiv:0803.0699](https://arxiv.org/abs/0803.0699) [[astro-ph](#)].
- [41] **The MAGIC** Collaboration, E. Aliu *et al.*, “Detection of pulsed gamma-rays above 25 GeV from the Crab pulsar,” [arXiv:0809.2998](https://arxiv.org/abs/0809.2998) [[astro-ph](#)].
- [42] J. Arons, “Pulsars as Gamma-Rays Sources: Nebular Shocks and Magnetospheric Gaps,” *Space Sci. Rev.* **75** (1996) 235–255.
- [43] **H.E.S.S.** Collaboration, F. Aharonian *et al.*, “First detection of a VHE gamma-ray spectral maximum from a Cosmic source: H.E.S.S. discovery of the Vela X nebula,” *Astron. Astrophys.* **448** (2006) L43–L47, [arXiv:astro-ph/0601575](https://arxiv.org/abs/astro-ph/0601575).
- [44] T. A. Porter and A. W. Strong, “A new estimate of the Galactic interstellar radiation field between 0.1 microns and 1000 microns,” [arXiv:astro-ph/0507119](https://arxiv.org/abs/astro-ph/0507119).